ACSNANO

www.acsnano.org

ARTICLE

Linear and Nonlinear Two-Terminal Spin-Valve Effect from Chirality-Induced Spin Selectivity

Tianhan Liu, Xiaolei Wang, Hailong Wang, Gang Shi, Fan Gao, Honglei Feng, Haoyun Deng, Longqian Hu, Eric Lochner, Pedro Schlottmann, Stephan von Molnár, Yongqing Li, Jianhua Zhao,* and Peng Xiong*

Cite This: *ACS Nano* 2020, 14, 15983−15991

Read Online

ACCESS | Metrics & More | Article Recommendations | Supporting Information

ABSTRACT: **Various mechanisms of electrical generation of spin polarization in *nonmagnetic* materials have been a subject of broad interest for their underlying physics and device potential in spintronics. One such scheme is chirality-induced spin selectivity (CISS), with which structural chirality leads to different electric conductivities for electrons of opposite spins. The resulting effect of spin filtering has been reported for a number of chiral molecules assembled on different surfaces. However, the microscopic origin and transport mechanisms remain controversial. In particular, the fundamental Onsager relation was argued to preclude linear-response detection of CISS by a ferromagnet. Here, we report definitive observation of CISS-induced magnetoconductance in vertical heterojunctions of (Ga,Mn)As/AHPA-L molecules/Au, directly verifying spin filtering by the AHPA-L molecules *via* spin detection by the (Ga,Mn)As. The pronounced and robust magnetoconductance signals resulting from the use of a magnetic semiconductor enable a rigorous examination of its bias dependence, which shows both linear- and nonlinear-response components. The definitive identification of the linear-response CISS-induced two-terminal spin-valve effect places an important constraint for a viable theory of CISS and its device manifestations. The results present a promising route to spin injection and detection in semiconductors without using any magnetic material.**

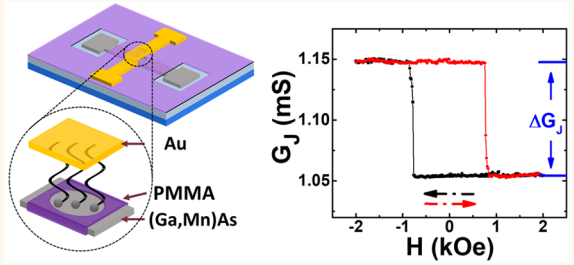

KEYWORDS: *molecular junction, chirality-induced spin selectivity, molecular spintronics, spin-valve effect, magnetic semiconductor, magnetoconductance*

There has been growing recent interest in electronic methods of producing spin polarization in semiconductors (SCs) *without* using any magnetic materials. One pathway is *via* spin−orbit interactions (SOIs) with which electron charge motion in a specific direction leads to spin polarization in an orthogonal orientation. Examples include spin Hall effect in III−V SCs[1−3] and spin-momentum locking in spin-helical surface states in 3D topological insulators.[4] Another scheme utilizes charge motion through materials exhibiting structural chirality in real space. The effect, termed chirality-induced spin selectivity (CISS),[5,6] has been reported in a variety of chiral molecules including dsDNA,[7,8] polypeptides,[9,10] and helicenes.[11] In contrast to solid state materials, organic molecules exhibit a rich variety of structures, which can be readily tailored to realize wide-ranging electronic properties and functionalities favorable for spintronics.[12] The experiments on CISS generally involve a self-assembled monolayer (SAM) of chiral molecules on a nonmagnetic noble metal. Spin filtering or spin selective transport of the electrons from the noble metal through the chiral SAM is evidenced in photoinduced charge transfer,[13] scanning conductance microscopy,[8] fluorescence microscopy,[14] and voltammetry[15] measurements. Spin polarization as high as 60% was measured at room temperature.[7] Besides chiral molecules, CISS was also predicted and/or observed in carbon nanotubes decorated with chiral molecules,[16−19] 2D chiral hybrid perovskites,[20,21] and superhelical conducting polyaniline microfibers.[22]

Received: September 3, 2020
Accepted: October 23, 2020
Published: November 2, 2020

https://dx.doi.org/10.1021/acsnano.0c07438
ACS Nano 2020, 14, 15983−15991

Theoretical studies of CISS have focused primarily on its microscopic origin, especially the relevance of SOI and molecular level structural details of the chiral molecules.[23−27] While the microscopic mechanism remains an important open issue,[5] modeling of the manifestation of CISS in practical transport devices was more scarce and inconsistent but has attracted significant recent interest. Two recent such studies[28,29] have highlighted the importance of the effects of the metal electrodes and their contacts with the molecules when modeling the magnetoconductance (MC) of chiral molecule junctions, which is expected to have contrasting manifestations in the linear- and nonlinear-response junction MC on the basis of the Onsager relation.

Experimentally, the device potential of CISS was demonstrated in a type of proof-of-concept memory device,[9,10] where the α-helical polyalanine was shown to be able to facilitate the magnetization reversal of a magnetic layer with or without electrical biasing. Another important class of devices involve *active electron transport through the chiral molecules*, resembling that in a magnetic tunnel junction or a spin valve. Conceptually, such a device should consist of a normal metal (NM) and a ferromagnet sandwiching a chiral molecule SAM, and CISS of the molecules would manifest in a MC corresponding to the magnetization reversal in the FM. Such a MC has been reported most commonly in the setup of conductance atomic force microscopy (cAFM)[8,11,30] and scanning tunneling microscopy,[31] which is not amenable to practical applications. Moreover, the conductance measurement depends to a large extent on the contact of the cAFM tip and a molecule, which leads to significant fluctuations and the necessity of relying on statistical averages of a great number of measurements. For the practical rendition of *planar* junctions, a critical obstacle is the well-known one in the field of molecular electronics: A SAM cannot serve as a flawless insulating barrier over practical device length scales, and any direct contact of the two metal electrodes through defects in the SAM essentially shorts out the device. To circumvent this problem, a common approach was to insert an oxide layer between the molecular SAM and a metal electrode.[9,11,32,33] Magnetoresistance (MR) was observed in cross-stripe planar junctions of Ni/Al_2O_3(MgO)/chiral molecules/Au with oligopeptides,[32] bacteriorhodopsin,[33] and helicenes[11] molecules. The observed MR tends to be small; moreover, the insertion of the oxide barrier may complicate the interpretation of the origin of the observed MR: Attributing the CISS in these devices to the chirality of the Al_2O_3 deposited onto the chiral molecules[32] contradicts the microscopic theories depending on internal structures of the chiral molecules.[23−27] Another approach employed a semiconductor as an electrode; for example, in a planar device the CISS-polarized electrons are detected with a GaN Hall sensor.[34]

Here, we report direct evidence for spin selective transport through chiral molecules assembled on a *ferromagnetic semiconductor* by measuring the MC of *vertical planar* junctions of (Ga,Mn)As/ α-helix L-polyalanine (AHPA-L) molecules/Au. The experiments were made possible by our ability to create high-quality SAMs and their micro-/nanopatterns on GaAs.[35,36] Replacing the ferromagnetic *metal* electrode in the magnetoresistive devices with the doped magnetic *semiconductor* presents the following advantages: (i) It eliminated the need for an oxide barrier. The Schottky barrier at the metal/SC direct contact effectively mitigates electrical shorts through defects in the SAM, as demonstrated in molecular junctions on p^+-GaAs.[37] (ii) The (Ga,Mn)As was grown to possess perpendicular magnetic anisotropy (PMA) for maximal interaction with, and unambiguous detection of, the perpendicularly polarized spin-filtered electrons. These two qualities enabled the observation of spin-valve MC distinctly associated with CISS in the two-terminal device. Most importantly, the robust spin-valve effect facilitated a comprehensive examination of the bias dependences of the MC, which yields definitive evidence for *both a nonlinear component and a nontrivial linear-response component in the MC*; the latter is the focus of a recent theoretical controversy.[38] The experiment also directly verifies the efficacy of CISS as a means for spin injection into a semiconductor without using any magnetic material.

RESULTS AND DISCUSSION

Panels a and b of Figure 1 show a schematic diagram and scanning electron microscopy (SEM) micrograph, respectively,

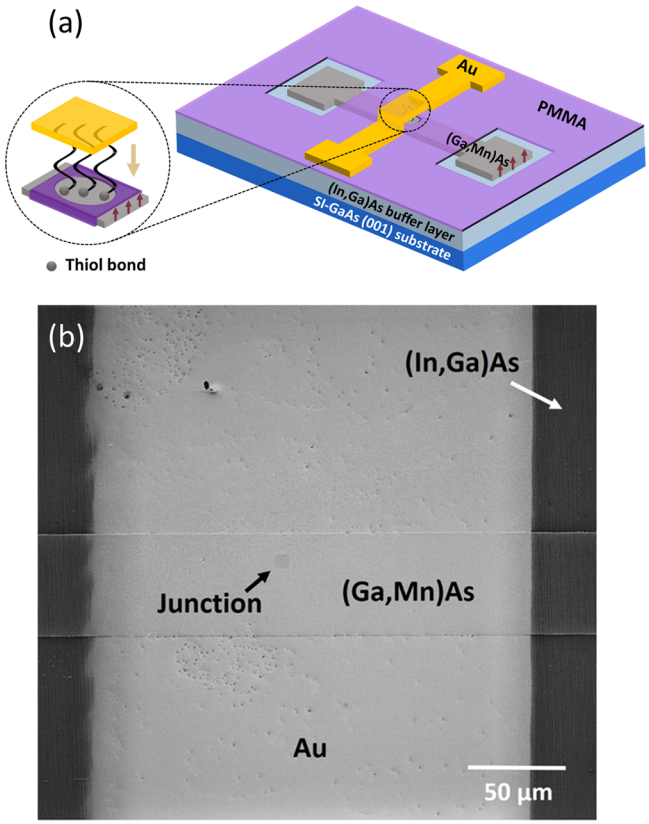

Figure 1. (a) Schematics of the device structure. The close-up image depicts the internal structure of a (Ga,Mn)As/AHPA-L molecules/Au vertical junction. The garnet arrows indicate the perpendicular magnetic anisotropy in the (Ga,Mn)As. The gold arrow indicates the spin polarization direction of the electrons through chiral molecules. AHPA-L molecules are assembled on (Ga,Mn)As with the thiol bond. (b) Scanning electron microscopy image of a 5 × 5 μm^2 junction.

of a vertical junction of (Ga,Mn)As/AHPA-L molecules/Au. Details of the experimental methods are described in Methods. The AHPA-L molecules, with length of 5.25 nm and an N-terminus with thiol, form covalent bonds with Ga and As,[35] facilitating the formation of SAM on (Ga,Mn)As. The AHPA-L molecules were assembled on MBE-grown epitaxial (Ga,Mn)As *via* solution assembly, and the resulting molecular layer was

https://dx.doi.org/10.1021/acsnano.0c07438
ACS Nano 2020, 14, 15983−15991

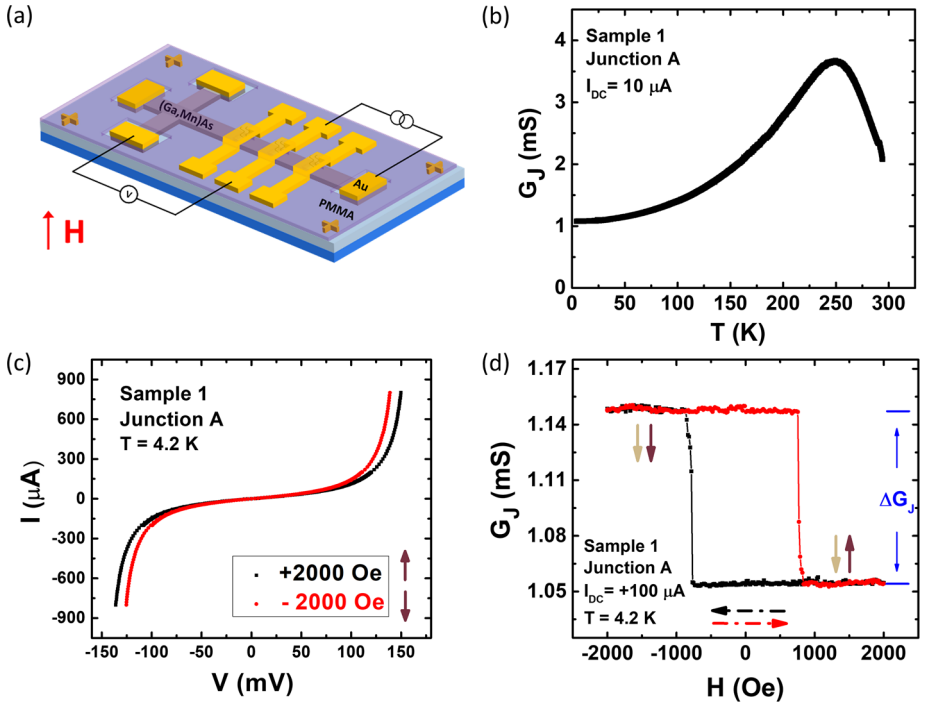

Figure 2. (a) Schematic diagram of the experimental setup for junction measurements. (b) Low-bias junction conductance as a function of temperature in zero applied magnetic field. (c) *I*−*V* characteristics of the junction in perpendicular magnetic fields of ±2000 Oe. (d) Junction conductance *versus* perpendicular magnetic field measured at a DC bias of 100 μA. Both the *I*−*V* and MC measurements show two distinct conductance states depending on the direction of the (Ga,Mn)As magnetization as indicated by the garnet arrows. The gold arrow indicates the direction of the electron spin polarization, which is independent of the magnetic field. The black and red dashed arrows indicate the sweeping direction of the magnetic field. Measurements in panels c and d were performed at 4.2 K.

measured *via* ellipsometry to have a thickness of 3.3 nm on GaAs. The result indicates that the molecules form a monolayer with the molecules tilting at an angle of 51° with respect to the normal, larger than the reported value of 40° on Au.[10]

The (Ga,Mn)As was grown by low-temperature MBE on an (In,Ga)As buffer layer; the resulting tensile strain leads to PMA.[39] The as-grown (Ga,Mn)As thin film used in this study has a Curie temperature of 140 K and coercive field of 460 Oe (Supporting Information Figure S1). The actual coercive fields of the (Ga,Mn)As in different devices varied from 180 to 460 Oe depending on the specific fabrication conditions they were subjected to. The devices were fabricated *via* a process consisting of photolithography and electron-beam lithography, Argon ion milling, AHPA-L SAM assembly, and top electrode evaporation. In Figure 1b, a close-up SEM image shows a 5 × 5 μm^2 junction in a fabricated device.

A schematic diagram of the magneto-electrical measurement setup for the (Ga,Mn)As/AHPA-L molecules/Au junctions is shown in Figure 2a. The specific junction resistance (RA product) values are on the order of 10^2 kΩ·μm^2, which are about an order of magnitude higher than the typical values for control junctions without the AHPA-L molecule SAM. Panels b and c of Figure 2 show a set of results from junction A in sample 1 of 10 × 10 μm^2. The zero-field low-bias junction conductance decreases with decreasing temperature at low temperatures and eventually saturates (Figure 2b). The general insulating behavior of the junction conductance and the high specific junction conductance at low temperature indicates significant coverage of the AHPA-L molecules on (Ga,Mn)As. It is also consistent with the quantitative estimation with the junction resistances with/without AHPA-L molecules (details in Supporting Information Note S1). The field-dependent *I*−*V* characteristics and perpendicular field MC of the junction were measured at low temperatures, and the results at 4.2 K are shown in Figure 2c,d, respectively. The *I*−*V* curves show strong nonlinear behavior, consistent with an asymmetric barrier which results in higher order contributions to the junction conductance.[40] A clear split was observed for the *I*−*V* curve when perpendicular magnetic fields of opposite polarities, ±2000 Oe, were applied. Since the applied fields were much above the coercive field of the (Ga,Mn)As, the two distinct conductance states are clearly associated with the reversed magnetization of the (Ga,Mn)As. This is evidenced directly in the MC measurements at fixed bias currents (100 μA in Figure 2d) while sweeping the perpendicular magnetic field.

Figure 2d shows a typical MC response in the form of sharp changes of the junction conductance coinciding with the coercive fields of the (Ga,Mn)As. The sharp conductance jumps are a result of the PMA in the strained (Ga,Mn)As. The dashed arrows refer to the directions of the field sweep for the red and black MC curves. Similar MC behavior was observed in 15 junctions in 7 different samples. We attribute the distinct two-state MC to a direct consequence of the CISS of AHPA-L molecules: The unpolarized electrons from the Au electrode attain spin polarization as they transport through the chiral molecules. The sign of the spin polarization depends only on the combination of the helicity of the molecules and current direction, and is independent of the external magnetic field, as depicted by the gold arrows in Figure 2d.[25,27] The (Ga,Mn)As, with high intrinsic spin polarization in the ferromagnetic state,[41] acts as a spin analyzer. As a result, the junction conductance changes as the magnetization of the (Ga,Mn)As is

https://dx.doi.org/10.1021/acsnano.0c07438
ACS Nano 2020, 14, 15983−15991

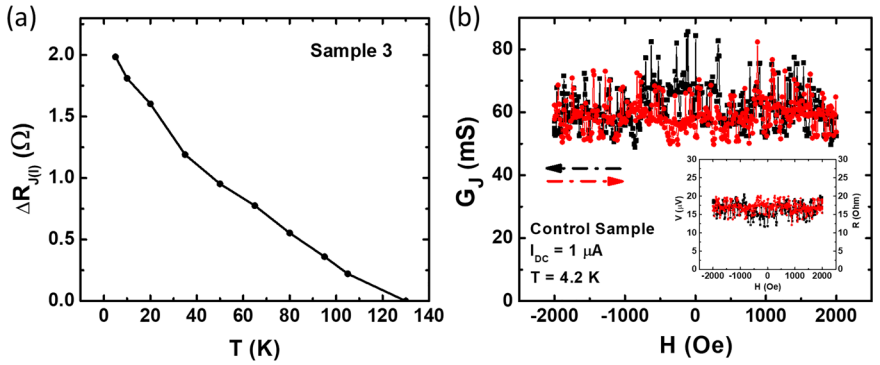

Figure 3. (a) $\Delta R_{J(I)}$ as a function of temperature. The data points were calculated on the basis of $\Delta R_{J(I)} = \frac{V_\uparrow - V_\downarrow}{I}$. Measurements were taken at 5, 10, 20, 35, 50, 65, 80, 95, 105, and 130 K. (b) Junction conductance *versus* perpendicular magnetic field of a control junction without chiral molecule SAM. No measurable MC is present. Inset: Measured junction voltage (resistance) *versus* magnetic field.

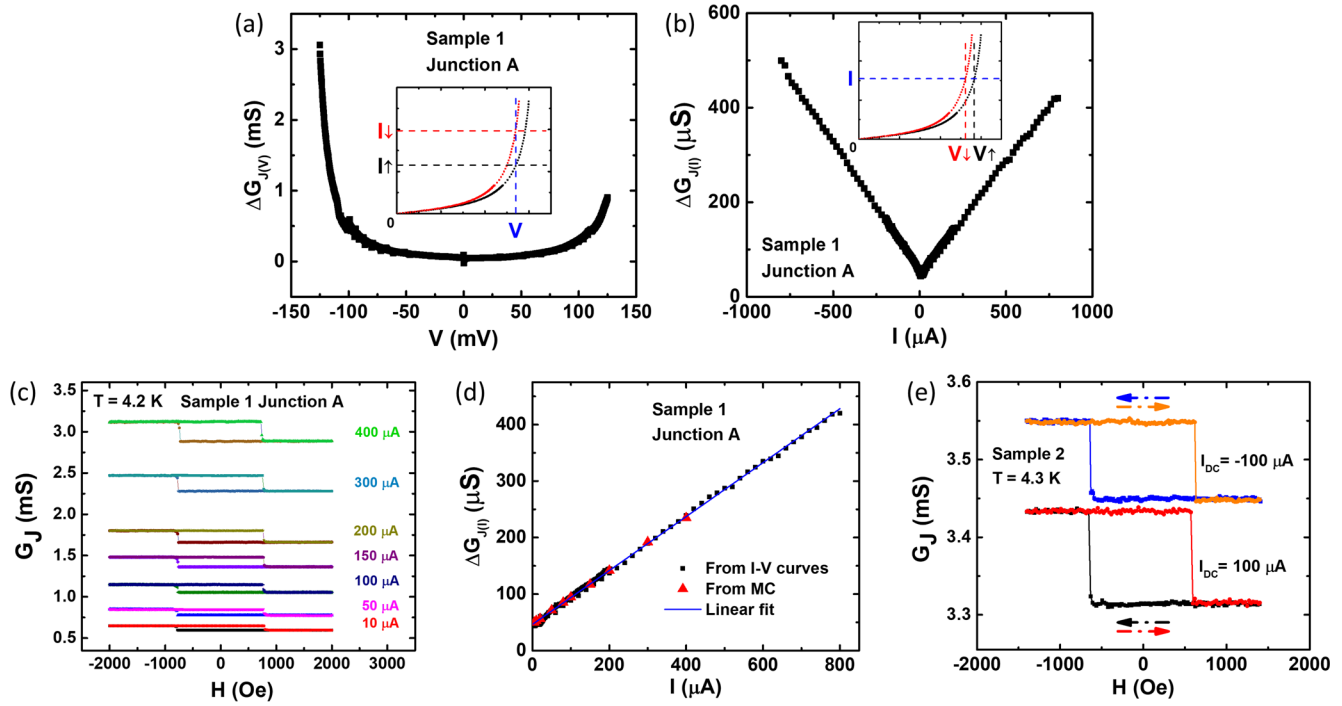

Figure 4. ΔG_J as a function of bias voltage (a) and bias current (b). The black squares in panels a and b are determined from the $I-V$ curves in Figure 2c, with fixed voltage and current, respectively. The respective insets illustrate how the data are extracted. (c) Representative MC curves measured at different bias currents. (d) Black squares from positive currents in panel b; red triangles from MC measurements at different bias currents (some shown in panel c); blue line a linear fit to the black squares. (e) MC curves for sample 2 at DC biases of 100 and −100 μA.

flipped. Here the percentage change of the junction conductance is about 9%; however, the junction conductance likely consists of parallel contributions from transport through the chiral molecules and defects in the SAM ((Ga,Mn)As/Au direct contact); hence, the absolute change of the junction conductance, ΔG_J, rather than the percentage change, is a more accurate measure of the CISS effect and is examined in detail below.

The low-temperature Hall resistance of the (Ga,Mn)As has an anomalous Hall component with field dependence similar to that of the junction MC (Supporting Information Figure S1c). However, it can be ruled out as the origin of the observed MC, as explained in detail in Supporting Information Note S2. Another effect that may contribute to the junction MC is that the chiral molecules may imprint weak ferromagnetism in the Au electrode.[42] Although there have been extensive reports of induced weak ferromagnetism at thiol−Au interfaces, direct spin-polarized tunneling measurements revealed no measurable spin polarization (<1%) at the interface.[43] Therefore, we do not believe either effect could account for the large MC observed in the devices in this work.

Figure 3a shows a representative temperature dependence of the junction MR. As expected, $\Delta R_{J(I)}$ decreases with increasing temperature and vanishes at the Curie temperature of the (Ga,Mn)As. Qualitatively, the decrease of $\Delta R_{J(I)}$ with increasing T is more rapid than that of the magnetization, which is consistent with the observation that the spin polarization in (Ga,Mn)As decreases with increasing T much faster than the magnetization.[44]

https://dx.doi.org/10.1021/acsnano.0c07438
ACS Nano 2020, 14, 15983−15991

In order to establish a definitive connection between the observed MC and electron transport through the chiral molecules, control devices were fabricated with the same process omitting the assembly of AHPA-L molecules on the junctions. The same set of measurements was performed in several different control samples, showing qualitatively similar results. The absence of distinct conductance states is shown directly in Figure 3b for a control junction; the junction conductance has no measurable changes at the coercive fields, and the value is about an order of magnitude larger than those of junctions with molecules. We emphasize that the seemingly high noise level in Figure 3b is due to a combination of low junction resistance and small measurement current (1 μA, so as to obtain the zero-bias response). The measured voltage and MR are plotted in the inset. The voltage noise level in the control junction is in fact similar to that in a junction with molecules (a direct comparison is presented in Supporting Information Figure S8). These results therefore point to the molecules as the origin of the observed spin-dependent MC in the molecular junctions.

It is also worth noting that although the molecular junctions contain a layer of organic molecules as a critical component, their electrical characteristics are very stable under ambient conditions. The measurements performed on a device after being stored in a desiccator at room temperature for four months yielded essentially the same results as those from measurements right after its fabrication (within a day). (See Figure S3 in the Supporting Information).

We now turn to the origin of the MC and its implications on the theoretical models. One most pertinent unsettled issue in the field is whether the CISS could lead to measurable spin-valve effect in a two-terminal device. Yang *et al.*[28] note that a spin−flip electron reflection process is inherent in the CISS transport in order to satisfy the Onsager relation. This implies a vanishing MC in the linear-response regime in a two-terminal junction of nonmagnetic-metal/chiral molecule/ferromagnet; rather, a four-terminal nonlocal scheme is required for the linear MC to materialize,[28] although a nonlinear MC is not precluded by the Onsager relation.[45] Dalum and Hedegård recently examined the spin-dependent electron transport of a similar system and reached the opposite conclusion.[29] They argue that SOI in the chiral molecules breaks the Onsager reciprocity and a new equilibrium state emerges with CISS-induced spin accumulation in the nonmagnetic lead. A nontrivial MC results from the emergent equilibrium state, which resembles that in a magnetic tunnel junction with two magnetic electrodes. In our devices, by measuring the bias dependences of the MC, we observed *both a pronounced nonlinear-response MC and a nontrivial linear-response MC*, as shown in Figure 4.

Analytically, Dalum and Hedegård calculated the electric current through the junction,[29] $I_\uparrow$ and $I_\downarrow$ (the arrows indicate the directions of the magnetization in the (Ga,Mn)As lead), based on the Landauer-Büttiker formalism. Upon magnetization reversal in the magnetic lead, $I_\uparrow$ and $I_\downarrow$ are different due to the difference in the induced magnetization from the spin accumulation in the nonmagnetic lead. Using the convention in ref 29,

$$I_{\uparrow\downarrow} = \int T^0_{LR}(1 \pm A\vec{m}\cdot\vec{a}_{\uparrow\downarrow})(n_F(E-\mu_L) - n_F(E-\mu_R))\frac{dE}{2\pi} \quad (1)$$

where T^0_{LR} is the transmission function between the magnetic and nonmagnetic leads satisfying the Onsager relation, A is a function related to SOI, $\vec{m}$ is the unit vector along the magnetic moment direction in the magnetic lead, and n_F is the Fermi−Dirac distribution (details in Supporting Information Note S4). $\vec{a}_\uparrow$ and $\vec{a}_\downarrow$ are the induced magnetizations from spin accumulation in the nonmagnetic lead for opposite magnetizations in the magnetic lead. Because of the CISS, $\vec{a}_\uparrow \neq -\vec{a}_\downarrow$, and the transmission coefficients for the opposite magnetizations, $T_{\uparrow\downarrow} = T^0_{LR}(1 \pm A\vec{m}\cdot\vec{a}_{\uparrow\downarrow})$, are different. Therefore, eq 1 implies two distinct conductance states depending on the magnetization direction of the magnetic lead, with the transition at the coercive field of the (Ga,Mn)As. This could be the origin of the nontrivial linear MC in our junctions, indicating that the idealized Onsager picture is not applicable to the two-terminal CISS devices.

The veracity of the model can be further tested from the dependence of the MC on the magnitude and direction of the current/voltage bias across the junction. Among the 15 junctions showing well-behaved MC, three junctions from two different samples were chosen for comprehensive detailed bias-dependence measurements. A set of experimental results from junction A in sample 1 are shown in Figure 4. The data in Figure 4a,b (black squares) are extracted from the $I-V$ curves in opposite saturation fields in Figure 2c, for fixed voltage and current, respectively (the ways the data are extracted are illustrated in the respective insets). The MR as a function of bias current, extracted from the same $I-V$ curves, is shown in Supporting Information Figure S7.

Figure 4a shows an approximately voltage independent finite MC at low biases, which rises sharply at biases coinciding with the turn-on voltage in the junction $I-V$. Each bias voltage corresponds to two different current states. From eq 1, we can derive an explicit expression for the bias-dependent MC:

$$\Delta G_{J(V)} = \frac{I_\downarrow - I_\uparrow}{V} = \int \alpha\Delta T\frac{dE}{2\pi} + V\int \beta\Delta T\frac{dE}{2\pi} + V^2\int \gamma\Delta T\frac{dE}{2\pi} \quad (2)$$

where $\mu_R - \mu_L = eV$, with V being the bias voltage across the junction, and α, β, and γ are energy- and temperature-dependent coefficients (details in Supporting Information Note S4). The finite zero-bias MC in Figure 4a is consistent with eq 2. The sharp rise at high biases implies that the higher order terms in eq 2 should be significant; however, quantitatively, the rapid increase of $\Delta G_{J(V)}$ at the turn-on voltage is closer to exponential than power law.

In contrast to the somewhat complex voltage dependence, $\Delta G_{J(I)}$ shows a striking linear dependence on the bias current, as shown in Figure 4b,d. Here, $\Delta G_{J(I)} = I\left(\frac{1}{V_\downarrow} - \frac{1}{V_\uparrow}\right)$. It is important to note that *the linear current dependence spans the entire bias range*, across the two distinct regimes in the voltage dependence. Qualitatively similar voltage and current dependences are observed in the other two junctions (shown in Supporting Information Figures S4 and S5).

The MC at different fixed currents can also be determined from full MC sweeps, and some representative MC curves are shown in Figure 4c. The $\Delta G_{J(I)}$ from these measurements are plotted as red triangles in Figure 4d, which are in excellent agreement with the black squares from the positive-bias $I-V$s

https://dx.doi.org/10.1021/acsnano.0c07438
ACS Nano 2020, 14, 15983−15991

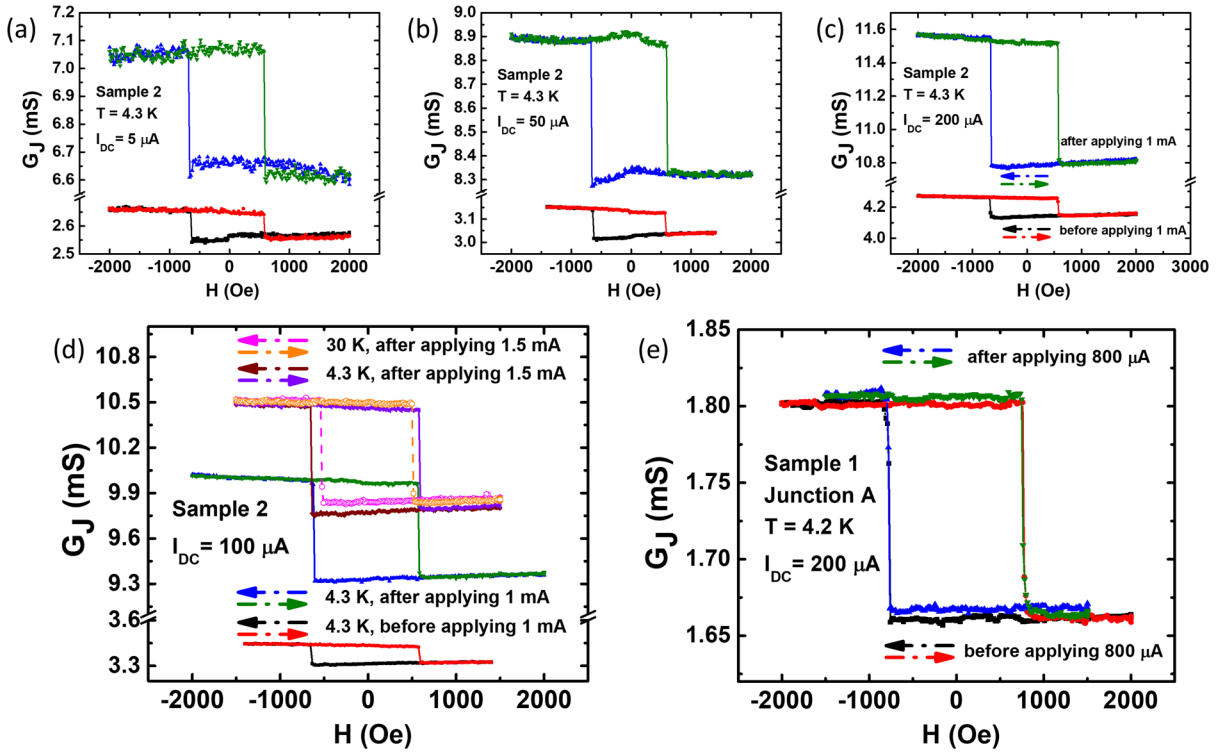

Figure 5. Junction MC measured at DC currents of (a) 5, (b) 50, and (c) 200 μA in sample 2, before (red and black curves) and after (orange and blue curves) *first-time* application of 1 mA bias current (55 mV) across the junction. The dashed arrows indicate the direction of the sweeping magnetic field. The notations in panel c also apply to panels a and b. (d) Junction MC measured at DC current of 100 μA before and after applying 1 mA, after applying 1.5 mA at 4.3 K and at 30 K. (e) Junction MC measured at DC current of 200 μA in sample 1 junction A, before and after first-time application of 800 μA bias current (140 mV) across the junction, showing no obvious change.

in Figure 3b. A linear fit to the current-dependence data (blue line) yields $\Delta G_{J(I)} = \Delta G_{J(0)} + aI$, where $\Delta G_{J(0)} = 46.2 \pm 0.4$ μS. Details of the error analysis of the linear fit of the bias dependences of the three junctions are shown in Supporting Information Figure S6. The value of $\Delta G_{J(0)}$ is consistent with the finite zero voltage bias value and constitute direct evidence that *a linear-response spin-valve-type MC is present in this two-terminal device*, although the higher order nonlinear contributions appear substantial.

Figure 4e shows MC for another junction at DC currents of opposite polarities, $\pm$100 μA, where +100 μA indicates the current flowing from the (Ga,Mn)As substrate to Au (electron injection from Au to (Ga,Mn)As) and vice versa. For this junction, a high-field hysteretic symmetric background is present, which has been subtracted to show ΔG_J clearly (details in Supporting Information Figure S10). Here, it is evident that the *reversal of the DC current direction does not change the junction conductance states*. However, it does change the magnitude of the MC slightly; specifically, $\Delta G_{J,I_+} = 0.118$ mS and $\Delta G_{J,I_-} = 0.101$ mS. This asymmetry is also apparent in Figure 4b between positive and negative currents. The asymmetry upon current reversal may be accounted for by the difference between electron injection from the nonmagnetic (Au) and magnetic ((Ga,Mn)As) electrode, as described in ref 29 and depicted in its Figure 3. The only modification that in (Ga,Mn)As the Fermi level is located closer to the top of the valence band does not change the qualitative picture. The overall junction conductance also shifts by 0.124 mS upon reversing the bias current, *i.e.*, $G_{J,I_+} - G_{J,I_-} = 0.124$ mS, where $G_{J,I_\pm}$ is the conductance at positive/negative DC currents. The differences between $\Delta G_{J,I_+}$ and $\Delta G_{J,I_-}$, and between G_{J,I_+} and G_{J,I_-}, are consistent with the presence of a first-order (odd) term in eq 2 and eq S4 (Supporting Information), respectively. The bias dependences of the MC, especially the striking linear current dependence, should place an important constraint on any theoretical model of the CISS-induced spin filtering and warrant further investigation.

Finally, we present an intriguing observation of variation of the MC in a junction in sample 2 after *first-time* application of large biases. Panels a–d of Figure 5 show the MC sweeps measured at 4.3 K and bias currents of 5, 50, 200, and 100 μA, respectively, before and after a large bias current of 1 mA (corresponding to a bias voltage of 55 mV), was applied on the junction. It is evident that after the application of the 1 mA current, both G_J and ΔG_J increase substantially. No discernible changes of G_J and ΔG_J were observed for applied biases up to 800 μA; namely, the G_J and ΔG_J changes occurred abruptly between bias currents of 800 μA and 1 mA applied to the junction. Furthermore, further increase of bias current beyond 1 mA resulted in little further changes. As demonstrated in Figure 5d, between 1 and 1.5 mA applied to the junction, ΔG_J (measured at 100 μA), showed no noticeable change, although G_J increased slightly. After the initial application of large bias currents, the junction is stable and does not relax back to the original state for the duration of the experiments (days); the stability was maintained at temperature of 30 K, as shown in Figure 5d. Detailed results of the variations of ΔG_J with application of large bias currents are described in Supporting Information Figure S5. It is informative to contrast these

https://dx.doi.org/10.1021/acsnano.0c07438
ACS Nano 2020, 14, 15983–15991

observations with the behaviors of sample 1, on which both junctions show no measurable changes in G_J and ΔG_J after application of biases as high as 800 μA, as shown in Figure 5e. We point out that although the 800 μA is smaller than the threshold current of 1 mA for sample 2, it in fact corresponds to a much larger voltage bias (140 mV), thus a much larger electric field, as the junction resistance is higher.

We conjecture that the observed changes of G_J and ΔG_J in the sample 2 junction and the differences with the sample 1 junctions may be due to variation of the quality in the initial assembly of the molecular layers in the two samples. In sample 2 after the device fabrication, the molecules may not be well aligned in some regions of the monolayer. The application of a sufficiently large electric field may align the molecules into an ordered monolayer, resulting in increases in both G_J and ΔG_J. For sample 1, both the coverage and quality of the molecular assembly are probably better; hence, G_J and ΔG_J of the two junctions in the sample are insensitive to a large applied electric field.

CONCLUSION

In summary, we have obtained direct evidence of CISS through chiral molecules assembled on a semiconductor surface. Experimentally, the CISS effect manifests in clear spin-valve signals in (Ga,Mn)As/AHPA-L molecules/Au junctions, resulting from spin filtering by the AHPA-L monolayer. Nontrivial linear- and nonlinear-response CISS-induced spin-valve signals are clearly identified in the two-terminal devices. The observation indicates that the ideal Onsager picture is not applicable to the linear transport regime in the two-terminal CISS devices, which should be accounted for in any viable theory for CISS and its device manifestations. With high-spin-filtering efficiency at room temperature,[7] the realization of CISS in SC-based two-terminal devices presents a promising nonmagnetic pathway to spin injection and detection in semiconductor spintronics.

METHODS

1. Materials and Sample Preparation. The AHPA-L in the experiments was purchased from RS Synthesis, LLC. It is based on α-helix L amino acids (H-CAAAA KAAAA KAAAA KAAAA KAAAA KAAAA KAAAA K-OH), where C, A, and K represent cysteine, alanine, and lysine. α-Helix has a right-hand-spiral conformation. The α-helix has 3.6 amino acids per turn of the helix, and the distance between each turn is 0.54 nm; thus, the length of the AHPA-L is $\frac{0.54}{3.6} \times 35 = 5.25$ nm. The cysteine in the N-terminus contains thiol. The AHPA-L molecules were dissolved in pure ethanol at 1 mM concentration. The solution was kept at −18 °C for storage.

The perpendicularly magnetized (Ga,Mn)As films were grown by MBE. A 500 nm thick (In,Ga)As buffer layer was first grown at 450 °C on semi-insulating (001) GaAs substrates. (Ga,Mn)As films of 40 nm thickness with perpendicular magnetic anisotropy were later grown at substrate temperature of 270 °C. The Curie temperature as-grown varies from 20 to 90 K depending on the Mn concentration (4% or 6%) and growth temperature. The carrier density is from 5×10^{20} to 1×10^{21} cm^{-3}. The Curie temperature increased from 90 K up to 144−149 K after annealing. The coercive field varies from 180 to 460 Oe depending on the annealing conditions.

For ellipsometry measurements, (Ga,Mn)As samples were first soaked in ammonium polysulfide solution at 50 °C for 5 min to remove the native oxide layer on the surface.[35] They were later left in the AHPA-L solution for 24 h for molecular self-assembly at room temperature. They were rinsed with ethanol and blown dry with nitrogen gas after the assembly.

2. Fabrication Process. The junction devices were fabricated in the following steps:

2a. (Ga,Mn)As Defined as Channel. The (Ga,Mn)As channel was first defined by photolithography. The sample was spin-coated with photoresist AZ5214E and prebaked at 110 °C for 50 s on a hot plate. It was later exposed under 350−500 nm UV light for 10 s and developed in a 1:5 solution of sodium-based AZ 351 developer diluted in DI water for about 2 min. After developing, the sample was postbaked at 120 °C for 60 s on the hot plate.

Then the electrode was etched by ion milling with an Ar ion beam produced by a 2 in. Kaufmann source. The Ar flow rate was 8.8 sccm, resulting in a pressure of 1.3×10^{-3} Torr. The discharge voltage was 62.5 V, the acceleration voltage was 210 V, and the beam voltage was 500 V. The cathode current was 6.8 A, and the beam current was 20 mA. Atomic force microscopy (AFM) measurements showed 73−76 nm etching depth with 7 min of milling.

2b. Au Contacts and Alignment Marks Deposited. A set of alignment marks was defined by photolithography with the same parameters as in step 2a. Cr (5 nm) and Au (20 nm) were then deposited by thermal evaporation, both at a rate of 1 Å/s. After the evaporation, the sample was immersed in acetone overnight for lift-off, followed by rinsing with acetone and isopropanol.

2c. Junctions Defined by Electron-Beam Lithography. The sample was spin-coated with 2% PMMA at 4 krpm for 30 s. It was prebaked at 180 °C for 10 min on a hot plate. The electron-beam lithography (EBL) was performed with an acceleration voltage of 20 kV and targeted dose of 160 μC/cm^2. For the small junction patterns, the spot size was 1.0, the step size was 0.01 μm, and the beam current was 0.0223 nA; for the large contact patterns, the spot size was 4.0, the step size was 0.05 μm, and the beam current was 0.825 nA, as measured by a Faraday cup. The sample was developed in methyl isobutyl ketone (MIBK) diluted with isopropanol (1:3) for 40 s and then in pure isopropanol for 30 s at room temperature.

2d. Oxide Layer on (Ga,Mn)As Removed and AHPA-L Assembled on Junctions. The sample was cleaned with O_2 plasma to remove any organic residue. It was set with medium power at 200 mTorr oxygen pressure for 1 min. The sample was then baked at 180 °C for 20 min on the hot plate to harden the PMMA. To remove the native oxide layer on the (Ga,Mn)As, the sample was etched with an ion mill for 1 min with the same parameters as in step 2a. It was immersed in ethanol immediately after being taken out from the ion mill chamber before the molecular assembly. Here, we chose a different method for oxide removal than the ammonium polysulfide passivation of (Ga,Mn)As used before,[35,36] as we noticed that the ammonium polysulfide tends to contaminate the surface after leaving the sample in the solution at 50 °C for 5 min.

For the assembly of AHPA-L monolayer on the (Ga,Mn)As, the sample was left in the AHPA-L solution at room temperature for 24 h. After the assembly, the sample was rinsed with ethanol and dried with nitrogen gas.

2e. Top Au Electrodes Deposited. A shadow mask was positioned on top of the sample by aligning the electrode patterns with the junctions under an optical microscope. For the evaporation, the same parameters as in step 2b were used in this step, except for the thickness of Au (50 nm). Also, the substrate was cooled with liquid nitrogen during the evaporation. The substrate temperature was maintained at −110 °C. It is informative to note that, in previous studies,[9,32] AlO_x was deposited onto the peptides which requires much harsher conditions than metal deposition, yet the chiral molecular structures were well-preserved. The metal deposition in our process should be even gentler. The liquid nitrogen cooling of the substrate was employed to further reduce the impact of the metal deposition on the molecules.

The control samples were fabricated in an identical process, except that in step 2d the sample was immersed in a pure ethanol instead of the AHPA-L molecule solution.

The samples were stored in a desiccator to minimize exposure to ambient moisture after fabrication.

3. Measurements. *3a. Electrical Measurements.* The sample was fixed on a socket with a copper base with GE vanish or photoresist

https://dx.doi.org/10.1021/acsnano.0c07438
ACS Nano 2020, 14, 15983−15991

and wired by hand with silver paint and Pt wire. The sample was measured within a few days after fabrication in a Janis ^{4}He cryostat and/or an Oxford ^{3}He cryostat. All of the measurements were performed at 4.2 K unless otherwise noted. Magnetic field perpendicular to the sample plane was applied up to 2000 Oe. The (Ga,Mn)As was first magnetized at 2000 Oe, and then the magnetic field was swept at a constant rate of 400 Oe/min for measurements. DC measurements were done with Keithley 2400 as the current source and HP 3458 as the voltmeter. AC measurements were performed with EG&G 124A and/or SR2124 dual-phase analog lock-in amplifiers. The sample was later measured at increased temperatures with similar procedure.

In the MC and $I-V$ measurements of the molecular junctions, Joule heating may become an issue at large bias currents, so the power was kept under 1 mW to avoid large temperature fluctuations. For example, bias current was kept below 1 mA for a junction of 1 kΩ. In $I-V$ measurements, the current is swept from negative to positive values with a current step of 20 μA and time interval of 1 s between each current step unless otherwise noted (more details in Supporting Information Figure S6).

In the calculations of $\Delta G_{J(V)}$ and $\Delta G_{J(I)}$, as described in the main text, the definitions are $\Delta G_{J(V)} = \frac{I_\downarrow - I_\uparrow}{V}$ and $\Delta G_{J(I)} = I\left(\frac{1}{V_\downarrow} - \frac{1}{V_\uparrow}\right)$. In both MC and $I-V$ measurements, currents are applied and voltages are measured so only $\Delta G_{J(I)}$ is the direct reflection from the experimental data. For $\Delta G_{J(V)}$, the $I-V$ curves are first interpolated to obtain the currents at the same voltage values and then used for the calculations of $\Delta G_{J(V)}$.

To measure the temperature dependence, the sample was cooled from 300 K to base temperature. The resistance was measured with DC current. For every 0.1 K change in temperature, positive and negative currents were applied to the sample. The resistance was determined to be the voltage difference divided by twice the applied current. The current reversal was necessary to eliminate the thermoelectric voltages along the circuit.

3b. Ellipsometry Measurements. The ellipsometry measurements were performed with an M-2000 spectroscopic ellipsometer. Five spots were chosen at random on two different oxide-free GaAs samples after the molecular assembly. The thickness of the monolayer was measured to be 3.3 nm for all spots.

ASSOCIATED CONTENT

Supporting Information

The Supporting Information is available free of charge at https://pubs.acs.org/doi/10.1021/acsnano.0c07438.

> Figures of thin film characterizations, molecular junctions' robustness, bias dependences, linear fitting and error analysis of the bias current dependences, sample 1 junction A MR, noise levels, and calculations for molecular coverage estimations; Schottky barrier width; theoretical model deviations of G_J and ΔG_J; explanation to rule out contribution from anomalous Hall effect in (Ga,Mn)As (PDF)

AUTHOR INFORMATION

Corresponding Authors

Jianhua Zhao − *State Key Laboratory of Superlattices and Microstructures, Institute of Semiconductors, Chinese Academy of Sciences, Beijing 100083, China; Beijing Academy of Quantum Information Science, Beijing 100193, China;* orcid.org/0000-0003-2269-3963; Email: jhzhao@semi.ac.cn

Peng Xiong − *Department of Physics, Florida State University, Tallahassee, Florida 32306, United States;* orcid.org/0000-0003-1746-1404; Email: pxiong@fsu.edu

Authors

Tianhan Liu − *Department of Physics, Florida State University, Tallahassee, Florida 32306, United States;* orcid.org/0000-0003-3934-0785

Xiaolei Wang − *State Key Laboratory of Superlattices and Microstructures, Institute of Semiconductors, Chinese Academy of Sciences, Beijing 100083, China;* orcid.org/0000-0002-6964-2453

Hailong Wang − *State Key Laboratory of Superlattices and Microstructures, Institute of Semiconductors, Chinese Academy of Sciences, Beijing 100083, China*

Gang Shi − *Beijing National Laboratory for Condensed Matter Physics, Institute of Physics, Chinese Academy of Sciences, Beijing 100190, China*

Fan Gao − *Beijing National Laboratory for Condensed Matter Physics, Institute of Physics, Chinese Academy of Sciences, Beijing 100190, China*

Honglei Feng − *Beijing National Laboratory for Condensed Matter Physics, Institute of Physics, Chinese Academy of Sciences, Beijing 100190, China*

Haoyun Deng − *Department of Physics, Florida State University, Tallahassee, Florida 32306, United States*

Longqian Hu − *Department of Physics, Florida State University, Tallahassee, Florida 32306, United States*

Eric Lochner − *Department of Physics, Florida State University, Tallahassee, Florida 32306, United States*

Pedro Schlottmann − *Department of Physics, Florida State University, Tallahassee, Florida 32306, United States*

Stephan von Molnár − *Department of Physics, Florida State University, Tallahassee, Florida 32306, United States*

Yongqing Li − *Beijing National Laboratory for Condensed Matter Physics, Institute of Physics, Chinese Academy of Sciences, Beijing 100190, China*

Complete contact information is available at: https://pubs.acs.org/10.1021/acsnano.0c07438

Notes

The authors declare no competing financial interest.

Liu, T.; Wang, X.; Wang, H.; Shi, G.; Gao, F.; Feng, H.; Deng, H.; Hu, L.; Lochner, E.; Schlottmann, P.; von Molnár, S.; Li, Y.; Zhao, J.; Xiong, P. Spin Selectivity through Chiral Polyalanine Monolayers on Semiconductors. *arXiv (AppliedPhysics)*, 2019, 2001.00097 https://arxiv.org/abs/2001.00097 (accessed 2020-01-03).

ACKNOWLEDGMENTS

We thank Kate Carnevale, Siwei Mao, Shucheng Tong, and Shengzhi Zhang for technical assistance. We acknowledge helpful discussions with Oren Ben Dor, Hanwei Gao, Zhilin Li, Yu Miao, Geoffrey Strouse, Qing-feng Sun, and David Van Winkle. The work at FSU is supported by NSF Grant DMR-1905843. The work at IOS is supported by the Strategic Priority Research Program of the Chinese Academy of Sciences (Grant Nos. XDB44000000 and QYZDY-SSW-JSC015) and the National Natural Science Foundation of China (NSFC Grant No. 11674312).

REFERENCES

(1) Kato, Y. K.; Myers, R. C.; Gossard, A. C.; Awschalom, D. D. Observation of the Spin Hall Effect in Semiconductors. *Science* **2004**, *306*, 1910−1913.

(2) Wunderlich, J.; Kaestner, B.; Sinova, J.; Jungwirth, T. Experimental Observation of the Spin-Hall Effect in a Two-

Dimensional Spin-Orbit Coupled Semiconductor System. *Phys. Rev. Lett.* **2005**, *94*, 047204.
(3) Garlid, E. S.; Hu, Q. O.; Chan, M. K.; Palmstrøm, C. J.; Crowell, P. A. Electrical Measurement of the Direct Spin Hall Effect in Fe/InGaAs Heterostructures. *Phys. Rev. Lett.* **2010**, *105*, 156602.
(4) Hasan, M. Z.; Kane, C. L. Colloquium : Topological Insulators. *Rev. Mod. Phys.* **2010**, *82*, 3045−3067.
(5) Naaman, R.; Waldeck, D. H. Spintronics and Chirality: Spin Selectivity in Electron Transport through Chiral Molecules. *Annu. Rev. Phys. Chem.* **2015**, *66*, 263−281.
(6) Naaman, R.; Paltiel, Y.; Waldeck, D. H. Chiral Molecules and the Electron Spin. *Nat. Rev. Chem.* **2019**, *3*, 250−260.
(7) Gohler, B.; Hamelbeck, V.; Markus, T. Z.; Kettner, M.; Hanne, G. F.; Vager, Z.; Naaman, R.; Zacharias, H. Spin Selectivity in Electron Transmission Through Self-Assembled Monolayers of Double-Stranded DNA. *Science* **2011**, *331*, 894−897.
(8) Xie, Z.; Markus, T. Z.; Cohen, S. R.; Vager, Z.; Gutierrez, R.; Naaman, R. Spin Specific Electron Conduction through DNA Oligomers. *Nano Lett.* **2011**, *11*, 4652−4655.
(9) Ben Dor, O.; Yochelis, S.; Mathew, S. P.; Naaman, R.; Paltiel, Y. A Chiral-Based Magnetic Memory Device without a Permanent Magnet. *Nat. Commun.* **2013**, *4*, 2256.
(10) Ben Dor, O.; Yochelis, S.; Radko, A.; Vankayala, K.; Capua, E.; Capua, A.; Yang, S.-H.; Baczewski, L. T.; Parkin, S. S. P.; Naaman, R.; Paltiel, Y. Magnetization Switching in Ferromagnets by Adsorbed Chiral Molecules without Current or External Magnetic Field. *Nat. Commun.* **2017**, *8*, 14567.
(11) Kiran, V.; Mathew, S. P.; Cohen, S. R.; Hernández Delgado, I.; Lacour, J.; Naaman, R. Helicenes-A New Class of Organic Spin Filter. *Adv. Mater.* **2016**, *28*, 1957−1962.
(12) Cornia, A.; Seneor, P. Spintronics: The Molecular Way. *Nat. Mater.* **2017**, *16*, 505−506.
(13) Abendroth, J. M.; Stemer, D. M.; Bloom, B. P.; Roy, P.; Naaman, R.; Waldeck, D. H.; Weiss, P. S.; Mondal, P. C. Spin Selectivity in Photoinduced Charge-Transfer Mediated by Chiral Molecules. *ACS Nano* **2019**, *13*, 4928−4946.
(14) Abendroth, J. M.; Nakatsuka, N.; Ye, M.; Kim, D.; Fullerton, E. E.; Andrews, A. M.; Weiss, P. S. Analyzing Spin Selectivity in DNA-Mediated Charge Transfer *via* Fluorescence Microscopy. *ACS Nano* **2017**, *11*, 7516−7526.
(15) Zwang, T. J.; Hürlimann, S.; Hill, M. G.; Barton, J. K. Helix-Dependent Spin Filtering through the DNA Duplex. *J. Am. Chem. Soc.* **2016**, *138*, 15551−15554.
(16) Diniz, G. S.; Latge, A.; Ulloa, S. E. Helicoidal Fields and Spin Polarized Currents in Carbon Nanotube−DNA Hybrids. *Phys. Rev. Lett.* **2012**, *108*, 126601.
(17) Alam, K. M.; Pramanik, S. Spin Filtering through Single-Wall Carbon Nanotubes Functionalized with Single-Stranded DNA. *Adv. Funct. Mater.* **2015**, *25*, 3210−3218.
(18) Alam, K. M.; Pramanik, S. Spin Filtering with Poly-T Wrapped Single Wall Carbon Nanotubes. *Nanoscale* **2017**, *9*, 5155−5163.
(19) Rahman, M. W.; Firouzeh, S.; Mujica, V.; Pramanik, S. Carrier Transport Engineering in Carbon Nanotubes by Chirality-Induced Spin Polarization. *ACS Nano* **2020**, *14*, 3389−3396.
(20) Lu, H.; Wang, J.; Xiao, C.; Pan, X.; Chen, X.; Brunecky, R.; Berry, J. J.; Zhu, K.; Beard, M. C.; Vardeny, Z. V. Spin-Dependent Charge Transport through 2D Chiral Hybrid Lead-Iodide Perovskites. *Sci. Adv.* **2019**, *5*, No. eaay0571.
(21) Huang, Z.; Bloom, B. P.; Ni, X.; Georgieva, Z. N.; Marciesky, M.; Vetter, E.; Liu, F.; Waldeck, D. H.; Sun, D. Magneto-Optical Detection of Photoinduced Magnetism *via* Chirality-Induced Spin Selectivity in 2D Chiral Hybrid Organic−Inorganic Perovskites. *ACS Nano* **2020**, *14*, 10370−10375.
(22) Jia, L.; Wang, C.; Zhang, Y.; Yang, L.; Yan, Y. Efficient Spin Selectivity in Self-Assembled Superhelical Conducting Polymer Microfibers. *ACS Nano* **2020**, *14*, 6607−6615.
(23) Yeganeh, S.; Ratner, M. A.; Medina, E.; Mujica, V. Chiral Electron Transport: Scattering through Helical Potentials. *J. Chem. Phys.* **2009**, *131*, 014707.
(24) Medina, E.; López, F.; Ratner, M. A.; Mujica, V. Chiral Molecular Films as Electron Polarizers and Polarization Modulators. *Europhys. Lett.* **2012**, *99*, 17006.
(25) Guo, A. M.; Sun, Q. F. Spin-Selective Transport of Electrons in DNA Double Helix. *Phys. Rev. Lett.* **2012**, *108*, 218102.
(26) Gutierrez, R.; Díaz, E.; Naaman, R.; Cuniberti, G. Spin-Selective Transport through Helical Molecular Systems. *Phys. Rev. B: Condens. Matter Mater. Phys.* **2012**, *85*, 081404.
(27) Guo, A.-M.; Sun, Q.-F. Spin-Dependent Electron Transport in Protein-Like Single-Helical Molecules. *Proc. Natl. Acad. Sci. U. S. A.* **2014**, *111*, 11658−11662.
(28) Yang, X.; van der Wal, C. H.; van Wees, B. J. Spin-Dependent Electron Transmission Model for Chiral Molecules in Mesoscopic Devices. *Phys. Rev. B: Condens. Matter Mater. Phys.* **2019**, *99*, 024418.
(29) Dalum, S.; Hedegård, P. Theory of Chiral Induced Spin Selectivity. *Nano Lett.* **2019**, *19*, 5253−5259.
(30) Bloom, B. P.; Kiran, V.; Varade, V.; Naaman, R.; Waldeck, D. H. Spin Selective Charge Transport through Cysteine Capped CdSe Quantum Dots. *Nano Lett.* **2016**, *16*, 4583−4589.
(31) Aragonès, A. C.; Medina, E.; Ferrer-Huerta, M.; Gimeno, N.; Teixidó, M.; Palma, J. L.; Tao, N.; Ugalde, J. M.; Giralt, E.; Díez-Pérez, I.; Mujica, V. Measuring the Spin-Polarization Power of a Single Chiral Molecule. *Small* **2017**, *13*, 1602519.
(32) Mathew, S. P.; Mondal, P. C.; Moshe, H.; Mastai, Y.; Naaman, R. Non-Magnetic Organic/Inorganic Spin Injector at Room Temperature. *Appl. Phys. Lett.* **2014**, *105*, 242408−5.
(33) Varade, V.; Markus, T.; Vankayala, K.; Friedman, N.; Sheves, M.; Waldeck, D. H.; Naaman, R. Bacteriorhodopsin Based Non-Magnetic Spin Filters for Biomolecular Spintronics. *Phys. Chem. Chem. Phys.* **2018**, *20*, 1091−1097.
(34) Fontanesi, C.; Capua, E.; Paltiel, Y.; Waldeck, D. H.; Naaman, R. Spin-Dependent Processes Measured without a Permanent Magnet. *Adv. Mater.* **2018**, *30*, 1707390.
(35) Wang, X.; Wang, H.; Pan, D.; Keiper, T.; Li, L.; Yu, X.; Lu, J.; Lochner, E.; von Molnár, S.; Xiong, P.; Zhao, J. Robust Manipulation of Magnetism in Dilute Magnetic Semiconductor (Ga,Mn)As by Organic Molecules. *Adv. Mater.* **2015**, *27*, 8043−8050.
(36) Liu, T.; Keiper, T.; Wang, X.; Yang, G.; Hallinan, D.; Zhao, J.; Xiong, P. Molecular Patterning and Directed Self-Assembly of Gold Nanoparticles on GaAs. *ACS Appl. Mater. Interfaces* **2017**, *9*, 43363−43369.
(37) Lodha, S.; Janes, D. B. Metal/Molecule/p-Type GaAs Heterostructure Devices. *J. Appl. Phys.* **2006**, *100*, 024503.
(38) Adagideli, İ.; Bauer, G. E. W.; Halperin, B. I. Detection of Current-Induced Spins by Ferromagnetic Contacts. *Phys. Rev. Lett.* **2006**, *97*, 256601.
(39) Thevenard, L.; Largeau, L.; Mauguin, O.; Patriarche, G.; Lemaître, A.; Vernier, N.; Ferré, J. Magnetic Properties and Domain Structure of (Ga,Mn)As Films with Perpendicular Anisotropy. *Phys. Rev. B: Condens. Matter Mater. Phys.* **2006**, *73*, 195331.
(40) Brinkman, W. F.; Dynes, R. C.; Rowell, J. M. Tunneling Conductance of Asymmetrical Barriers. *J. Appl. Phys.* **1970**, *41*, 1915−1921.
(41) LeClair, P. R.; Tsymbal, E. Y.; Mryasov, O. N. Spin-Dependent Tunnelling in Magnetic Tunnel Junctions. *J. Phys.: Condens. Matter* **2003**, *15*, R109−R142.
(42) Carmeli, I.; Leitus, G.; Naaman, R.; Reich, S.; Vager, Z. Magnetism Induced by the Organization of Self-Assembled Monolayers. *J. Chem. Phys.* **2003**, *118*, 10372−10375.
(43) Zhang, X.; McGill, S. A.; Xiong, P.; Wang, X.; Zhao, J. Probing the Thiol-Gold Planar Interface by Spin Polarized Tunneling. *Appl. Phys. Lett.* **2014**, *104*, 152403.
(44) Yu, G. Q.; Chen, L.; Rizwan, S.; Zhao, J. H.; Xu, K.; Han, X. F. Improved Tunneling Magnetoresistance in (Ga,Mn)As/AlO_x/CoFeB Magnetic Tunnel Junctions. *Appl. Phys. Lett.* **2011**, *98*, 262501.
(45) Yang, X.; van der Wal, C. H.; van Wees, B. J. Detecting Chirality in Two-Terminal Electronic Nanodevices. *Nano Lett.* **2020**, *20*, 6148−6154.

https://dx.doi.org/10.1021/acsnano.0c07438
ACS Nano 2020, 14, 15983−15991